

Wavelet Analysis of Atmospheric Turbulence over a Coral Reef Flat

ANDREW WIEBE AND ANDREW STURMAN

Centre for Atmospheric Research, University of Canterbury, Christchurch, New Zealand

HAMISH MCGOWAN

Climate Research Group, School of Geography, Planning and Environmental Management, The University of Queensland, Brisbane, Queensland, Australia

(Manuscript received 21 April 2010, in final form 22 December 2010)

ABSTRACT

The world's tropical coral reefs are at risk of severe bleaching episodes and species decline in response to global climate variability. The ecological and economic value of reef ecosystems is enormous, yet very little is known of the physical interactions that take place at the coral–ocean–atmosphere interfaces. This paper introduces and validates a novel technique for the acquisition of surface energy balance measurements over Heron Reef, part of the Capricorn Bunker Group of the southern Great Barrier Reef, Australia. Measurements of surface energy and radiation exchanges were made using a Campbell Scientific eddy covariance (EC) measurement system mounted on a floating pontoon anchored to the reef flat. A Nortek Vector velocimeter was positioned next to the pontoon to record wave motion. Wavelet analysis techniques were used to decompose the turbulent exchange of sensible heat measured by the EC unit and to compare vertical velocity measurements with wave-induced motion recorded by the velocimeter. The results indicate that although the EC system and the velocimeter share intermittent periods of high common power in their respective wavelet variance spectra, these regions are not coherent and differ in strength by more than an order of magnitude. It was concluded that over a standard averaging period of 30 min the wave-induced motion of the pontoon would not significantly interfere with the acquisition and calculation of turbulent fluxes of sensible and latent heat, thereby confirming the robustness of this method of obtaining surface energy balance measurements over coral reefs.

1. Introduction

Current estimates of global climate change indicate that increases in sea surface temperature (SST) of 1°–3°C above the current annual mean and rises in mean sea level of $0.13 \pm 0.006 \text{ mm yr}^{-1}$ will occur over the next century (Solomon et al. 2007). This poses a serious risk to the global distribution of coral reefs because they are limited by SST and water depth (Hoegh-Guldberg 1999; Lesser 2004). Importantly, these predicted changes in marine conditions are believed to increase the frequency and location of mass bleaching events, where corals eject their algal symbionts in response to changes in key environmental variables (Hoegh-Guldberg et al. 2007). The

most important variable determining the occurrence of mass bleaching events is a sustained elevation of SST above the maximum monthly mean by approximately 1°C (Hoegh-Guldberg 1999; Berkelmans 2002). To date no known comprehensive studies of coral reef surface energy budgets (SEBs) have been undertaken. The complex interaction of key environmental variables, such as water temperature and depth, turbidity, and the exchanges of sensible and latent heat between the atmosphere and water surface that alter bleaching thresholds, has not been explored in any detail (Smith 2001; Berkelmans 2002). As such, a joint study between the University of Canterbury's Centre for Atmospheric Research and the University of Queensland's Climate Research Group was initiated to investigate the processes that control the thermal environment of the reef flat at Heron Island (Fig. 1; 23°26'S, 151°55'E). Heron Island is one of over 300 coral cays found within the Great Barrier Reef complex and is located approximately 80 km offshore from the central

Corresponding author address: Andrew Sturman, Private Bag 4800, Department of Geography, University of Canterbury, Christchurch 8140, New Zealand.
E-mail: andrew.sturman@canterbury.ac.nz

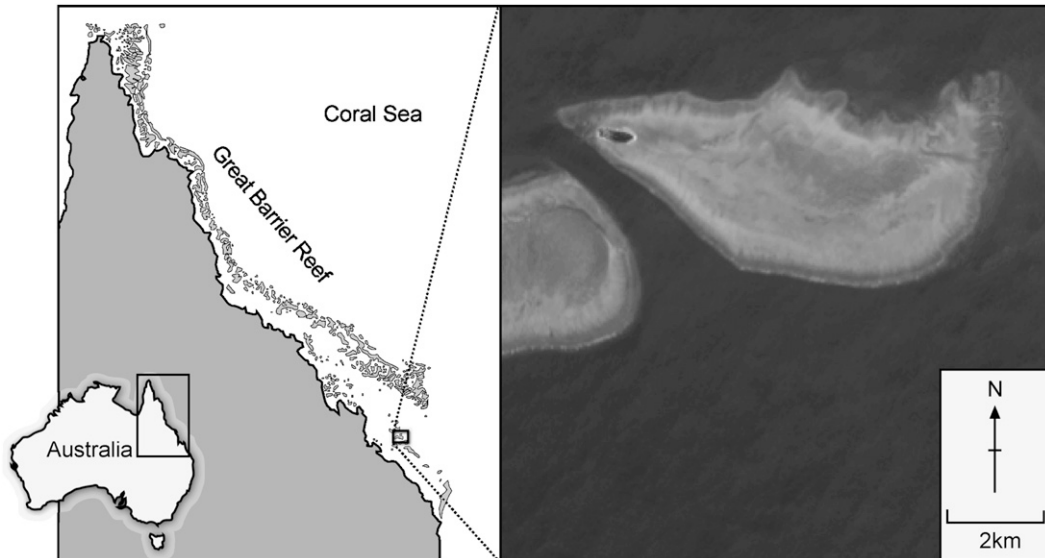


FIG. 1. Heron Island and the Great Barrier Reef complex. Heron Island is one of six islands that make up the Capricorn Bunker Group, the southernmost portion of the Great Barrier Reef. [Image modified from http://svs.gsfc.nasa.gov/vis/a000000/a003300/a003343/ikonos_heron_island_lrg_web.png.]

Queensland coast. Heron Reef, which covers 27 km², is considered typical of the platform reefs of the southern Great Barrier Reef.

A key challenge to obtaining SEB measurements from floating platforms over a reef flat (or any water surface) is to account for the role of wave action on the measurement of turbulent fluxes. Turbulence can be defined as a state of fluid flow in which the instantaneous velocities exhibit irregular and apparently random fluctuations that are capable of transporting atmospheric properties, such as heat, moisture, and momentum (Oke 1987). The fluctuation of the vertical velocity about its mean value (w') is the result of turbulence that forms eddies of varying sizes (Stull 1998; Oke 1987). These eddies are known to be of two general types—attached and detached (Townsend 1976; Perry et al. 1986; Perry and Li 1990).

Attached eddies constitute large-scale organized structures responsible for the transfer of energy and, hence, other atmospheric properties (scalars) between the surface and overlying atmosphere, while detached eddies are less organized small-scale structures that have little or no interaction with the surface. Coherent structures can be thought of as repeated well-organized cycles of ejection-like upwelling flow and sharp sweep-like descending motions (Gao and Li 1993), where intensified transfer of scalars can occur within short-lived events (bursts; Baldocchi and Meyers 1988). The presence of coherent structures in the atmospheric boundary layer (ABL) has since proved to play a central role in the transport of heat, moisture, and momentum between the surface and the

atmosphere, accounting for nearly 80% of the total energy exchange (Baldocchi and Meyers 1988; Gao and Li 1993; Szilagyi et al. 1999).

The main aim of this paper is to show how wavelet analysis techniques can be used to address concerns associated with making energy flux measurements from a floating platform. In doing so, it also illustrates some of the complexity in the energy exchanges between the atmosphere and ocean surfaces. Determining the SEB and parameterizing the transfer of momentum and heat over coral reefs is vital to the understanding of ocean–reef–atmosphere interactions and determining the future responses of these systems to global climate change. This paper therefore introduces and validates a novel technique for the acquisition of surface energy balance measurements over coral reef flats.

2. Methods

a. Pontoon eddy covariance system

The eddy covariance (EC) system consisted of a three-dimensional sonic anemometer (model CSAT-3; Campbell Scientific, Logan, Utah) with a measurement resolution of $u_x, u_y = 1 \text{ mm s}^{-1} \text{ rms}$, $u_z = 0.5 \text{ mm s}^{-1} \text{ rms}$, speed of sound = $15 \text{ mm s}^{-1} (0.025^\circ\text{C}) \text{ rms}$, and a krypton hygrometer (model KH20; Campbell Scientific) mounted on a floating pontoon (Fig. 2). The pontoon was positioned over an area of mixed coral and sand patches off the southeastern end of Heron Island ($23^\circ 26.573\text{S}$, $151^\circ 55.203\text{E}$). The EC system operates by measuring the

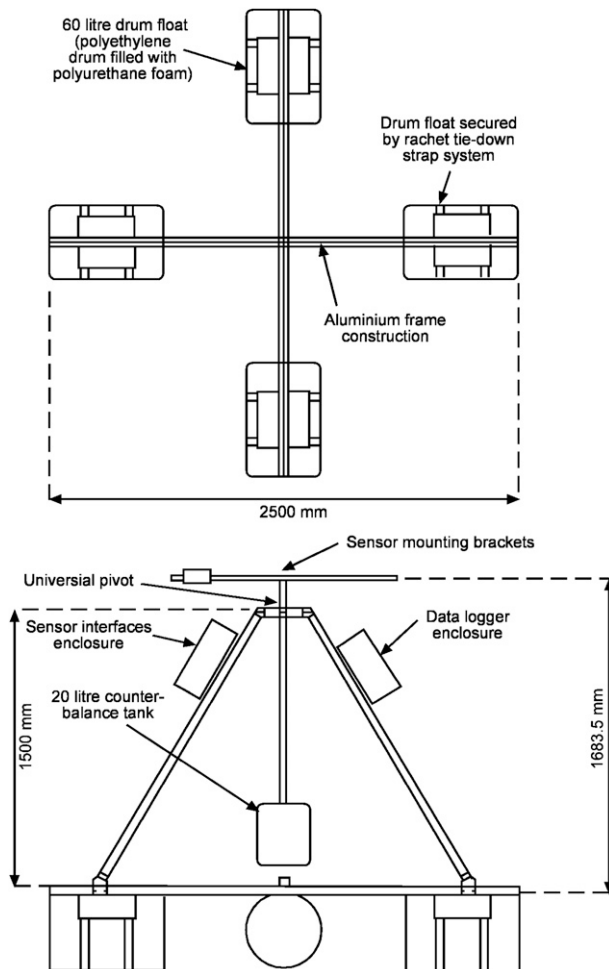


FIG. 2. Schematic drawing of the floating pontoon.

instantaneous fluctuations of the three orthogonal wind vectors (u , v , and w), the speed of sound as it travels from one axial head of the CSAT-3 to another from which the virtual temperature (T_v) is deduced, and the specific humidity (q) at the sampling frequency (10 Hz is used in this study). The system provides a direct measurement of the energy fluxes between a surface and the overlying atmosphere.

One of the key environmental variables for coral survival is water depth (Hoegh-Guldberg 1999; Lesser 2004). As such, measurement of surface fluxes required that the EC system remain at the same height above the surface (2 m). This posed a unique problem as the surface in this case was semiexposed corals at low tide and up to 2 m of water at high tide. Hence, a floating platform was constructed that was capable of carrying the instrumentation, as well as power sources and datalogger.

The pontoon consisted of a fixed frame for mounting batteries and solar panels, while the measurement

instrumentation was mounted on booms extending beyond the footprint of the pontoon. The instrument booms were fixed to a central rod weighted at the base and fixed with elastic cords to the frame. The central rod was capable of axial movement via a universal pivot joint at the attachment point to dampen any oscillatory influence of water waves on the structure. To validate this measurement technique a Nortek Vector (model NO-1351 RUD, Nortek AS, Rud, Norway) velocimeter was positioned in the water in close proximity ($23^{\circ}26.572\text{S}$, $151^{\circ}55.203\text{E}$) to the pontoon. In addition to making precise water velocity fluctuations, the velocimeter is capable of measuring sea surface fluctuations via an inbuilt pressure (p) transducer at a sampling frequency of 8 Hz. The Nortek has a measurement accuracy of $\pm 0.5\%$ of measured value $\pm 1 \text{ mm s}^{-1}$. Both systems were programmed to simultaneously burst sample all raw data for 12 min at 30-min intervals in an attempt to determine the influence of wave motions on the quantities measured by the EC unit.

A 12-min sampling interval was chosen for both practical and empirical reasons. First, the storage capacity for raw data at 10 Hz becomes very large after this time period and consumes a significant amount of battery power. This proved to be a vital issue because access to the pontoon to replace batteries and download data was restricted to low tide and, of course, the batteries were not being recharged by the solar panels once night fell. Second, recent studies by Sun et al. (2006) and Voronovich and Kiely (2007) have confirmed that sampling periods greater than 5 min are sufficient to capture all the frequencies of flux contributing perturbations in the atmosphere, where flux bias was less than instrument error (4%) when averaged over a 10-month period. The sampling period extended for 2 days (10–11 February 2007, hereafter referred to as Julian days 41 and 42) to enable comparison between daytime and nocturnal fluxes.

b. Wavelet analysis

Wavelets are two-dimensional localized transformations that retain information about the temporal location of frequencies by isolating the scale contribution of individual events in space (Katul and Vidakovic 1998; Salmund 2005). The technique consists of projecting the signal onto a set of wavelet functions. These functions are derived from a “mother” wavelet by a series of dilations and translations to produce “daughter” wavelets. Thus, the wavelet transform adjusts its analyzing window to match the frequency (e.g., a short window for high frequencies and a long window for low frequencies). This allows for a better localization of structures in space and time, replacing frequency with a time-scale representation that is more suitable for examining the characteristics of coherent structures in the atmospheric boundary layer (Farge 1992;

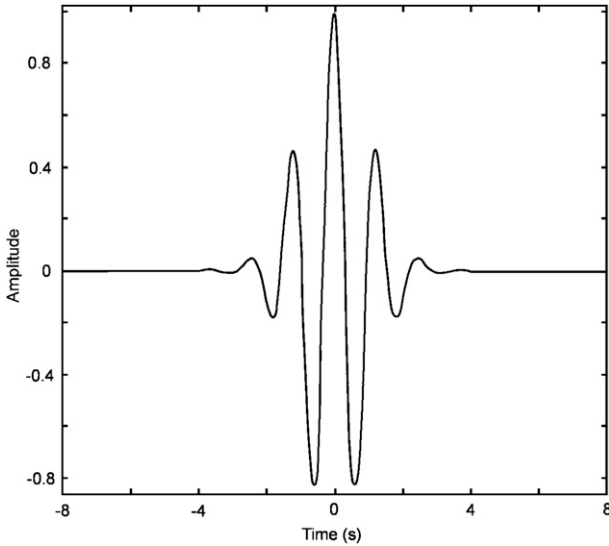


FIG. 3. The Morlet wavelet used as a bandpass filter by the continuous wavelet transform for determination of the wavelet variance (power) and the extraction of coherent structures.

Kumar and Foufoula-Georgiou 1994; Hagelberg and Gamage 1994).

There are two types of wavelet transforms—the discrete wavelet transform (DWT) and the continuous wavelet transform (CWT). The DWT is useful for data compression and noise reduction, while the CWT is better suited for feature extraction (Grinsted et al. 2004; Domingues et al. 2005) and was used in this study. The CWT of a time series (χ_n) is given by Torrence and Compo (1998) as

$$W_n(s) = \sum_{n'=0}^{N-1} \chi_{n'} \Psi^* \left[\frac{(n' - n)\delta t}{s} \right], \quad (1)$$

where $\Psi^*(t)$ is the complex conjugate of the wavelet function, N is the number of points in the time series, δt is the time step, n is the localized time index, and s is the wavelet scale (the width of the analyzing wavelet), resulting in locally scaled wavelet coefficients $W_n(s)$. By varying s and translating along n , the amplitude of any structures within the time series is located by the scale and any variations of the amplitude through time are extracted (Torrence and Compo 1998). In this study, the Morlet CWT (Fig. 3) was employed because it retains coherency at the edge of sharp boundaries, effectively defining the beginning of any change in conditions (Hagelberg and Gamage 1994). The Morlet wavelet is given by Torrence and Compo (1998) as

$$\Psi_0(\eta) = \pi^{-1/4} e^{i\omega_0\eta} e^{-\eta^2/2}, \quad (2)$$

where ω_0 is the dimensionless frequency (in this case 6), η is the dimensionless time, and e is the energy. The

CWT [Eq. (1)] applies the wavelet [Eq. (2)] as a bandpass filter to the time series. The relationship between the wavelet scale and Fourier period is approximately equal, such that period = $1.03 \times$ scale, making use of the two terms interchangeable (Torrence and Compo 1998). Wavelet variance (equivalent to a Fourier power spectrum) is then defined from the wavelet coefficients as the mean of the absolute wavelet coefficients squared (Torrence and Compo 1998), that is,

$$|W_n(s)|^2, \quad (3)$$

which, when integrated over time, yields the global wavelet energy spectrum, also termed the wavelet variance, which gives the energy content at the defined scales (Farge 1992). This allows for the characteristic duration of an event to be visualized as a global maximum peak in the spectrum corresponding to a certain time scale. The CWT is limited by the fact that it is not completely localized in time, and hence generates boundary artifacts at the ends of the time series. To counter this effect a cone of influence (COI) is introduced to the wavelet expansion as the area outside of which wavelet power drops to e^{-2} (where e is given by $\sqrt{2s}$). This is at the end of the time series, where values are outside the COI and can be ignored as artifacts of the technique and not related to any physical processes (Torrence and Compo 1998). The statistical significance of the wavelet power spectrum can be tested against a red noise background generated by a first-order autoregressive (AR1) process. Thereby, if a peak in the wavelet power spectrum is significantly above this background spectrum, then it can be assumed to be a real physical feature with a certain percentage of confidence (Grinsted et al. 2004). As with Fourier spectral analysis it is sometimes beneficial to compare the power spectrum of the two time series. This is accomplished by using the cross-wavelet transform (XWT) given by Torrence and Compo (1998) as

$$\frac{|W_n^X(s) W_n^{Y*}(s)|}{\sigma_X \sigma_Y} \Rightarrow \frac{Z_\nu(p)}{\nu} \sqrt{P_k^X P_k^Y}, \quad (4)$$

where $W_n^X(s)$ and $W_n^{Y*}(s)$ are the continuous wavelet transforms of the two time series, the asterisk denotes the complex conjugate, σ_X and σ_Y are the standard deviations of the two time series, and $Z_\nu(p)$ is the confidence level associated with the probability (p) for a probability density function defined by the square root of the product of two chi-squared (χ^2) distributions. In addition, for $\nu = 1$ (real wavelets) $Z_1(95\%) = 2.182$, while for $\nu = 2$ (complex wavelets) $Z_2(95\%) = 3.999$; P_k^X and P_k^Y are the theoretical Fourier spectra of the two time series where regions with high common power in

time–frequency space are extracted. The cross-wavelet phase angle between components of two time series is a useful indication of causal relationships. The circular mean (α_m) of the phase angle is taken from regions within the XWT that are above the 95% confidence level of significance and outside of the COI. This allows the difference in the relationship of the two time series to be quantified, with the 95% confidence interval taken as the error. This is a generally accepted method for calculating the circular mean of a set of angles ($\alpha_1, I = 1, \dots, n$), defined by Grinsted et al. (2004) as

$$\alpha_m = \arg(X, Y) \quad \text{with} \quad X = \sum_{i=1}^n \cos(\alpha_i) \quad \text{and} \\ Y = \sum_{i=1}^n \sin(\alpha_i), \quad (5)$$

where a linear cause-and-effect relationship between two components would result in a mean phase angle of approximately 0° (Grinsted et al. 2004). With the XWT one can now calculate the wavelet coherence (WTC), given by Grinsted et al. (2004) as

$$R_n^2(s) = \frac{|S[s^{-1}W_n^{XY}(s)]|^2}{S[s^{-1}|W_n^X(s)|^2]S[s^{-1}|W_n^Y(s)|^2]}, \quad (6)$$

where S is a smoothing operator (in this case 0.6), which is similar to a correlation coefficient, only localized in time–frequency space, and s is the wavelet scale that is linearly related to the characteristic period of the wavelet (Jevrejeva et al. 2003). The WTC identifies areas of locally phase-locked behavior, even at low power. The smoothing operator is an empirically derived constant for each wavelet; details can be found in Torrence and Compo (1998). Statistical significance is determined by Monte Carlo methods using an AR1 background spectrum. This is accomplished by generating 10^3 AR1 time series and computing their Fourier power spectrum (P_k) with a lag-1 autocorrelation (a) estimated from the observed time series, given by Grinsted et al. (2004) as

$$P_k = \frac{1 - a^2}{|1 - ae^{-2i\pi k}|^2}, \quad (7)$$

where k is the Fourier frequency index.

3. Data analysis

Forty sampling periods were obtained from 1000 LST on Julian day 41 to 0530 LST on Julian day 42, with water depth varying from about 0.36 to 1.33 m at the pontoon site. The unfiltered w and p values were first normalized by subtracting the mean and dividing by their respective standard deviations. Because the velocimeter

was acquiring data at 8 Hz, to directly compare its wavelet spectrum with that of w' both of the datasets were block averaged down to 2 Hz. This is a feasible option because the coherent structures in w' are expected to be below this frequency and the loss of high-frequency detached eddies should not significantly affect the results (Thomas and Foken 2005, 2007). In wavelet analysis the maximum allowable time scale must be the next power of 2 below half the length of the time series. Because the atmospheric sampling period was for 12 min (720 s), the maximum wavelet scale was set at 256 s decreasing by powers of 2 to the lowest resolvable scale (Δj) of $2\Delta t$ (≈ 0.5), with 12 suboctaves per scale resulting in a total of 97 individual wave forms.

The next step was to apply the CWT [Eq. (1)] using the Morlet wavelet [Eq. (2), Fig. 3] to the prepared w' and p' time series and calculate their global wavelet variance [Eq. (4)]. Levels of significant wavelet variance (using the 95% confidence level) were calculated by comparison against an AR1 red noise background. All 40 sampling periods were sorted into day (from 0600 to 1800 LST), night (from 1800 to 0600 LST), and composite spectra were produced for each time period (Fig. 4). The CWTs of the filtered w' and p' were then passed through the XWT and WTC calculations (Figs. 5 and 6). The computation of the CWT, XWT, WTC, and global wavelet variance was carried out in Matlab version 7.4a following the methods outlined by Torrence and Compo (1998), Thomas and Foken (2005), and Grinsted et al. (2004) using scripts written by Torrence and Compo (1998; available online at <http://paos.colorado.edu/research/wavelets/>) and Grinsted et al. (2004; available online at <http://www.pol.ac.uk/home/research/waveletcoherence>). Determining the strength of any interference from water pressure fluctuations (p') on the measurement of w' required that the individual wave forms, ranging from the 2- to 32-s scale for both time series, be summed and averaged (Figs. 7 and 8). This produced one wave form indicative of the coherent structure containing portion of the w' time series and the subsequent p' time series, which was then subtracted from w' . The filtered w' wave form was then subtracted from the original time series, so that no interference would result in zero fluctuations over the sampling period, and plotted over the unfiltered w' time series (Figs. 7c and 8c).

4. Results

Wavelet analysis of w' and p'

The wavelet variance spectra obtained from the CWT transformation of w' exhibit distinct maxima above the 95% significance level (dashed line in Fig. 4) in only the daytime period. These maxima were located at 1.5 s

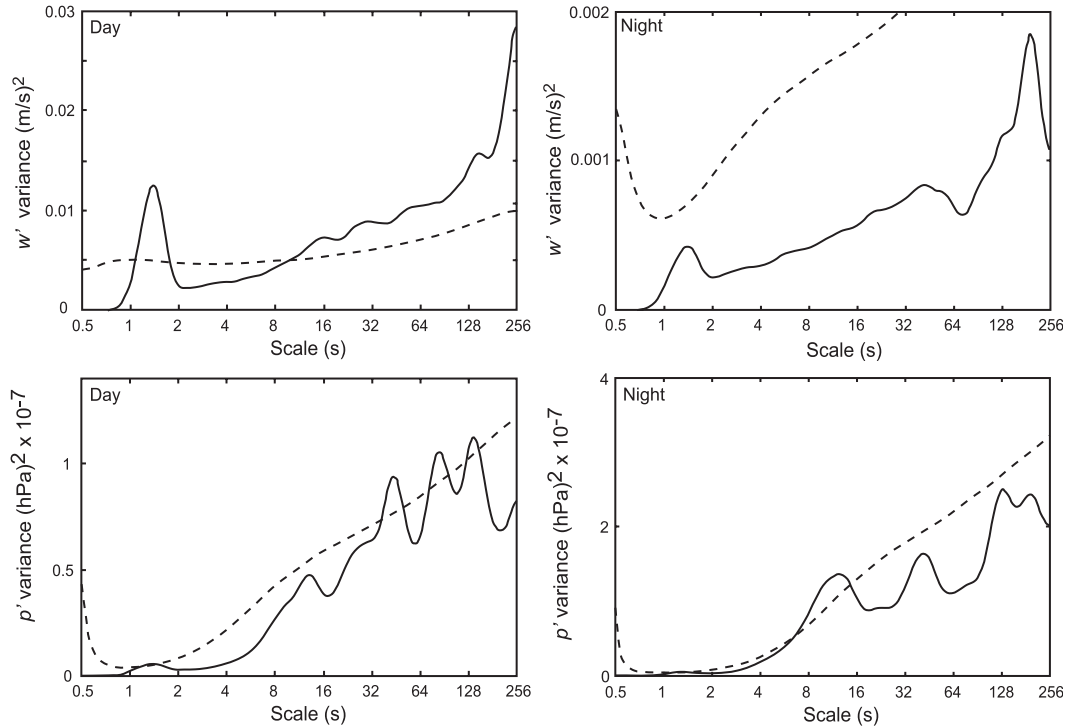


FIG. 4. Wavelet variance spectrum for (top) w' and (bottom) p' . The absolute variance (solid line) and the 95% significance level against lag-one autoregressive red noise (dashed line) are shown. See the text for a detailed description of the spectral analysis.

[$0.013 W_n(s)^2$] and 256 s [$0.029 W_n(s)^2$] during daytime, although the spectrum from about 10 to 256 s is all significant at 95% (Fig. 4). When the w' and p' variances (power) are mapped to wavelet space using the CWT, the equivalent of a Fourier spectrogram is produced; only, in this case, it is termed a scalegram (Figs. 5 and 6). This type of visualization allows one to view regions of significant variance in relation to real time and the scale at which they occurred. As with the variance spectrum graphs (Fig. 4), significance was determined by comparison with lag-1 AR1 red noise, with 95% values represented by regions encircled by a thick black line in Figs. 5 and 6. The curved black line entering from the top edges of the CWT projection represents the COI, whereby the data not encased by this line are considered dubious and should not be used for interpretation. This holds for all subsequent projections. The grayscale bar to the right of the projection is a relative scale of wavelet variance from weak ($1/32$) to strong (32). The spectral peaks found in the daytime variance graphs are clearly outlined in the scalegram with almost continuous effects on flow in the 1–2-s scale of w' (Fig. 5 b), with significant bursts of energy occurring occasionally at the 8–16-s scale, along with a significant region between the 64- and 128-s scale in the first half of the time period. The WTC determines how coherent the XWT is in time–frequency

space. This can be thought of as a localized correlation coefficient between the two wavelet-transformed time series. The statistical significance of the WTC is estimated using Monte Carlo methods (refer to section 2).

The wavelet variance spectrum for p' exhibited significant maxima at 1.5 s [$0.56 \times 10^{-8} W_n(s)^2$], 48 s [$0.943 \times 10^{-7} W_n(s)^2$], 90 s [$1.057 \times 10^{-7} W_n(s)^2$], and 145 s [$1.133 \times 10^{-7} W_n(s)^2$] during the day, and about 1.5 s [$0.052 \times 10^{-7} W_n(s)^2$] and 13 s [$1.35 \times 10^{-7} W_n(s)^2$] during the night. These results are indicative of the principal time scales of water height fluctuations at the pontoon site and are also reflected in the patterns of significant fluctuations shown in Figs. 5a and 6a.

The XWT of w' and p' for the daytime period exhibits periodic regions of significant common variance that vary between being in phase (arrows pointing to the right) and antiphase (arrows pointing the left), and having w' lead p' (arrows pointing up), and w' lag p' (arrows pointing down; see Figs. 5 and 6). If the two signals were indeed linked one would expect the arrows to point in the same direction for a given scale or range of scales. Figure 5c clearly shows that the signals are not phase locked, but instead fluctuate between states, indicating that p' is not linked to w' . A similar result was found for the nighttime XWT, where areas of significant high common power were exhibited, but no significant

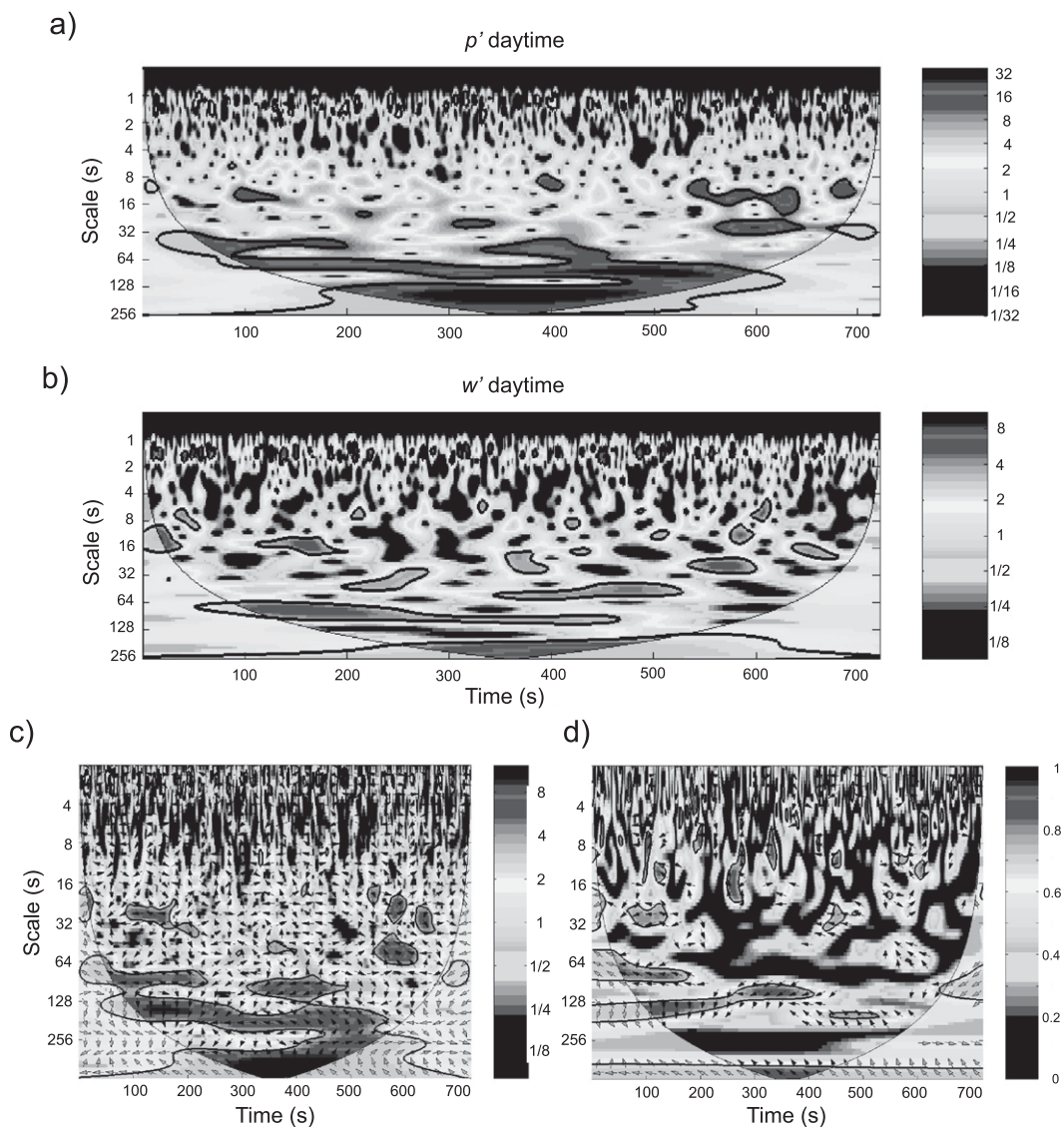


FIG. 5. CWT for (a) pressure and (b) vertical velocity fluctuations, (c) XWT, and (d) WTC for the 2-Hz w' and p' time series during daytime. The CWT projection is similar to a Fourier spectrogram where peak variance (power) is mapped by scale and location in time. The XWT displays regions of significant common high variance (encircled by thick black line) between the two time series. In the WTC, areas of significant coherence are denoted as per the XWT. The descending curved line at the edges of all projections is the COI and the grayscale bars on the right-hand side of (a)–(c) display the relative amplitude of the variance, while the grayscale bar in the WTC is a measure of coherence, where “1” equals perfect coherence.

relationship between them can be observed (Fig. 6c). The WTC projection for the daytime observation period does not exhibit any appreciable area of significant coherence (Fig. 5d). There are two regions worth noting: one occurring between the 16- and 32-s scale, showing antiphase coherence at the beginning of the period, and the other occurring at the 64–128-s scale. The nighttime WTC shows far fewer coherent regions, with the most significant being a region of in-phase coherence at the 16- and 48-s scale at a time of 600–650 s (Fig. 6d). In

theory, once coherence is achieved between two variables this should propagate throughout the time scale (Grinsted et al. 2004). This does not occur between w' and p' . Even though regions of high common power coincide they are not locally correlated, so wave action should not significantly affect the measurements made by the pontoon EC unit. This conclusion is supported by the summed and averaged individual waveforms for the 2–32-s scales for two selected day and night periods, where the difference between the original w' and the

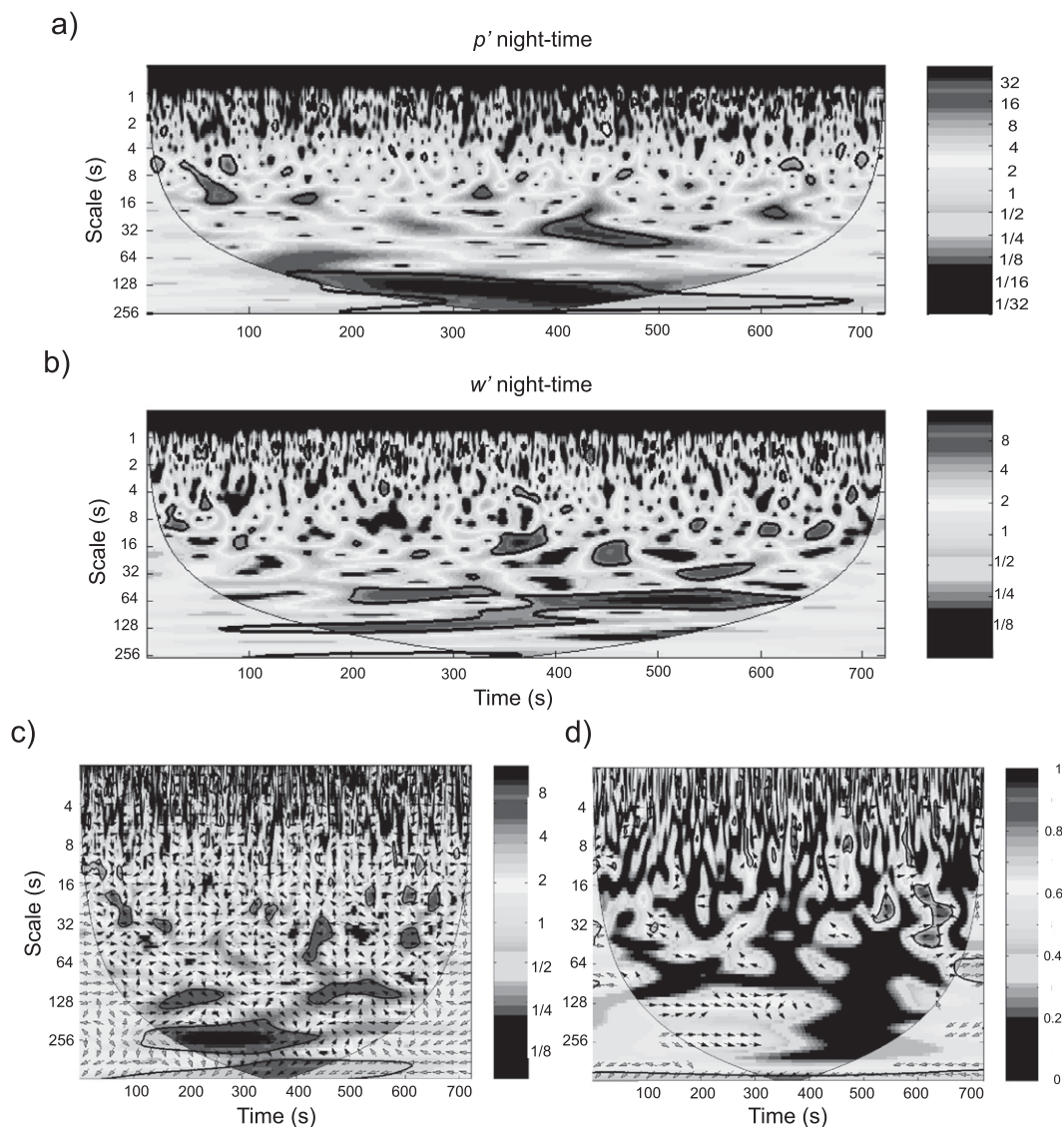


FIG. 6. CWT for (a) pressure and (b) vertical velocity fluctuations, (c) XWT, and (d) WTC for the 2-Hz filtered p' and w' time series during nighttime. Significant areas of common high power occur between the 8- and 32-s scales, although they are not significantly coherent. Refer to the text for a detailed description.

filtered w' time series is at least an order of magnitude smaller than the measured flux (Figs. 7c and 8c). The CWT, XWT, and WTC routines were performed on a total of 40 sampling periods—15 daytime and 25 nighttime—with consistent results. Figure 9 shows the mean ratio (and 5th and 95th percentiles) between w' and the difference shown in Figs. 7c and 8c, plotted for each half-hour time period. The values indicate that the effect of p' is consistently at least an order of magnitude smaller than the fluxes; over a 30-min averaging period that would be negligible. Not surprisingly, the ratio during the day shows greater variability than that at night. This would be expected because the wind speed is

generally higher during the day, with more associated turbulence. The relevant factor is that the influence on the measured w' is relative to its magnitude because this is a coupled system and wave fluctuations are driven by wind, so that the larger the wave fluctuation, the larger the w' in the atmosphere. Hence, the influence of p' remains small relative to the magnitude of w' .

5. Discussion

a. Pontoon eddy covariance

Results of the wavelet analysis show that the movement of the pontoon did not exert a significant influence

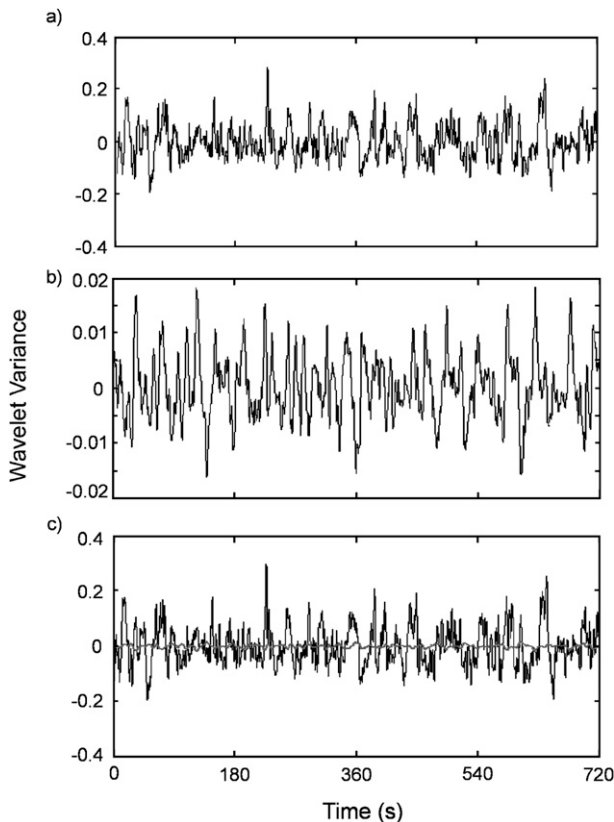


FIG. 7. Summed and averaged wave forms for 2–32-s scales for (a) w' and (b) p' at 1400 LST on Julian day 41; (c) p' was then subtracted from w' and the difference is shown as the thicker line fluctuating around the center line.

on the measurement of w' by the EC system or the detection of coherent structures. Although the spectra of w' and p' did show regions of common high power, they were not coherent. The collocation of common power is to be expected because the wave field is generated in part by the exchange of momentum from the atmosphere to water (Stull 1998). Interaction between the two spectra was at least an order of magnitude below the measured fluctuations, so that over an averaging period of 30 min the small-scale perturbations of wave-induced motion are expected to be filtered out and subsequent calculations of sensible heat flux can be considered to accurately reflect turbulent energy fluxes. The floating pontoon EC system therefore appears to be a sound and robust method for investigating the surface energy exchanges at the reef–ocean–atmosphere interface. This conclusion is also supported by comparing data collected by the floating pontoon with data collected by a second eddy covariance system located on a nearby beach for a period when the winds were onshore (so that both systems were measuring fluxes over the reef flat). Figure 10 shows that the variation of the sensible heat

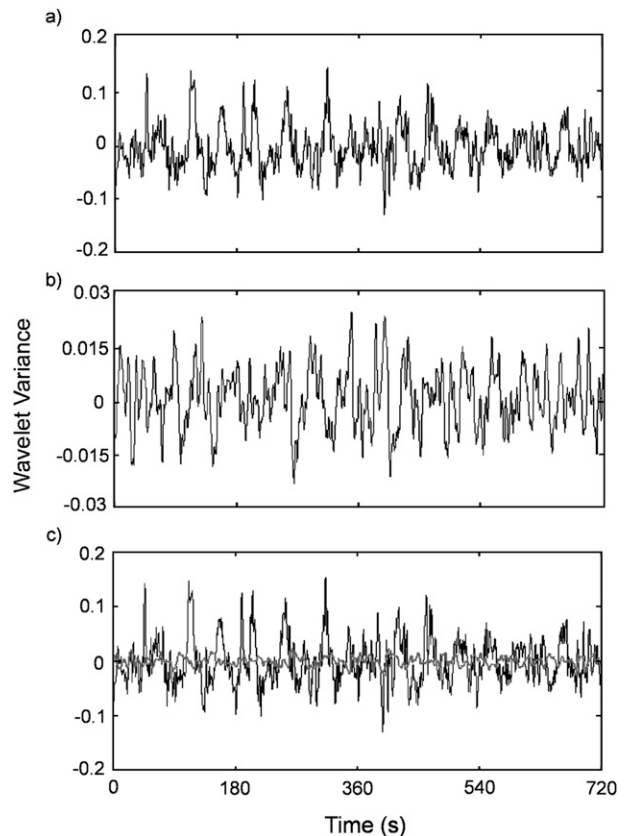


FIG. 8. Summed and averaged wave forms for 2–32-s scales for (a) w' and (b) p' at 0200 LST on Julian day 42; (c) p' was then subtracted from w' and the difference is shown as the thicker line fluctuating around the center line.

fluxes measured by the two eddy covariance systems is very similar.

This measurement system provides a novel and relatively unintrusive way of acquiring quality data without the damage to coral outcrops required by tower-mounted units. The system also introduces a degree of mobility, where the pontoon can be easily maneuvered to different locations or brought ashore in the event of severe weather. Importantly, this system allows EC measurements to be made at near-constant height above the water surface throughout the tidal cycle. The system is limited by the fact that some form of wave data is required to validate the results. However, a multidisciplinary approach is required to study the reef environment, including the measurement of current and wave characteristics. One issue of the measurement technique that requires further refinement is the positioning and choice of wave recorder employed. Ideally, this should be positioned directly under the pontoon. In this study, the water beneath the pontoon was too shallow, necessitating that the velocimeter be positioned to one side. This introduces

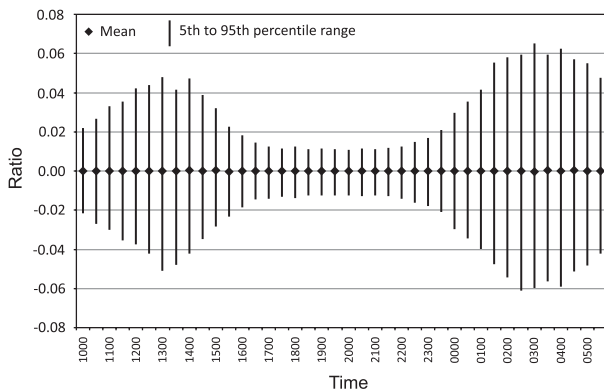


FIG. 9. The mean ratio between w' and the difference between w' and p' shown in Figs. 7c and 8c, and 5th and 95th percentiles, plotted for each half-hour time period.

a possible lag time between the measured w and p fluctuations. Also, the model of the velocimeter that was used was designed primarily for directional current measurements, with water depth (waves) as an additional variable. In the future, a dedicated wave meter would be advisable, although the three-dimensional current velocity data could also be analyzed to assess the extent to which wave-induced vertical motion in the water is linked to turbulence in the atmosphere above.

b. Wavelet analysis

As one might expect, not all wavelets are the same. The Morlet wavelet used here is well localized in time and does a good job of computing wavelet variances. However, it is limited in its ability to extract individual features from the time series. In this respect, the Haar wavelet is better suited. It becomes apparent that the use of one wavelet, or even restricting oneself to either the continuous or discrete variety, can impose undue limits on the capability of the technique itself. Perhaps a more sensible approach would be to use a suite of wavelets for filtering, decomposition, and spectral derivation. This raises another issue with the use of wavelets, which is the a priori selection of the “mother” wavelet, presumably for its suitability for the task at hand. The subjective specification of wavelet transforms can have a significant impact on the interpretation of localized events associated with turbulent activity (Katul and Vidakovic 1996). Fortunately, several objective methodologies have been put forward to address this issue (Donoho and Johnstone 1994, Szilagy et al. 1999). The computation of the XWT also poses some interesting issues because the required smoothing function can have the effect of reducing the potential for feature extraction, which would appear to defeat the original purpose of wavelet analysis (Torrence and Compo 1998).

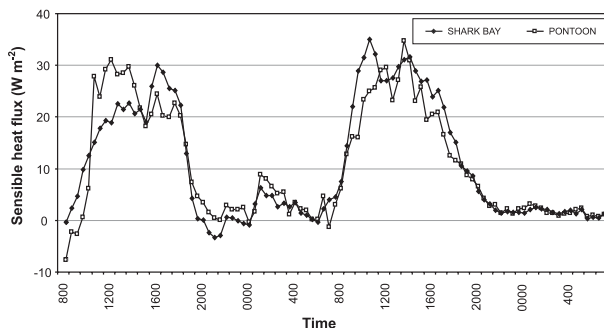


FIG. 10. Comparison of sensible heat flux measured by eddy covariance systems on the beach at Shark Bay and offshore on the pontoon, 9–11 Feb 2007.

6. Conclusions

This study introduced a novel application of the eddy covariance measurement system and detailed the use of wavelet analysis in validating the data collected by this technique. The pontoon-mounted EC system proved to be a sound method of acquiring surface energy balance measurements, probably largely due to the shallow layer of water in which it was deployed. The unobtrusive nature and mobility of the system provides a much needed alternative to tower-mounted units, allowing the application of energy balance studies to such remote and sensitive areas as coral reef ecosystems. The results indicate that minor fluctuations in the location of the EC system relative to the water surface does not appear to significantly affect w' measurements because of the different time scales of atmospheric turbulence and pontoon motion. Effects of movement of the pontoon can easily be filtered out of the signal provided the intrusive waveform is known.

This paper represents a preliminary step toward developing a thorough knowledge of the turbulent exchanges of heat, moisture, and carbon dioxide at the reef–ocean–atmosphere interface. It will be followed by a series of papers examining actual measurements of the turbulent fluxes over coral reefs obtained using the floating pontoon under a range of conditions, and investigating the surface–atmosphere processes that impact the environment experienced by the coral itself. To the authors’ knowledge there is no empirically derived parameterization of the surface energy balance and turbulent exchanges of such scalars over coral reefs in the current range of global circulation models, or their downscaled counterparts. The description and proper characterization of turbulent energy transfer processes are vital to understanding turbulence generation and its influence on surface–atmosphere exchanges (Zeng et al. 1993).

Acknowledgments. This study would not have been possible without the funding and technical support provided by the Department of Geography, University of Canterbury and the School of Geography, Planning and Environmental Management, The University of Queensland. The authors thank Dr. Deirdre Hart, Dr. David Neil, and Miss Mellissa Mackellar for their assistance with field measurements, and extend a special thank you to Dr. Jennifer Salmond for advice regarding the application of wavelets to atmospheric datasets. The staff of the Heron Island Research Station is also thanked for their assistance during this study.

REFERENCES

- Baldocchi, D. D., and T. P. Meyers, 1988: Turbulent structure in a deciduous forest. *Bound.-Layer Meteor.*, **43**, 345–365.
- Berkelmans, R., 2002: Time-integrated thermal bleaching thresholds of reefs and their variation on the Great Barrier Reef. *Mar. Ecol. Prog. Ser.*, **229**, 73–82.
- Domingues, M. O., O. Mendes, and A. Mendes da Costa, 2005: On wavelet techniques in atmospheric sciences. *Adv. Space Res.*, **35**, 831–842.
- Donoho, D. L., and I. M. Johnstone, 1994: Ideal spatial adaptation by wavelet shrinkage. *Biometrika*, **81**, 425–455.
- Farge, M., 1992: Wavelet transforms and their applications to turbulence. *Annu. Rev. Fluid Mech.*, **24**, 395–457.
- Gao, W., and B. L. Li, 1993: Wavelet analysis of coherent structures at the atmosphere–forest interface. *J. Appl. Meteor.*, **32**, 1717–1725.
- Grinsted, A., J. C. Moore, and S. Jevrejeva, 2004: Application of the cross wavelet transform and wavelet coherence to geophysical time series. *Nonlinear Processes Geophys.*, **11**, 561–566.
- Hagelberg, C. R., and N. K. K. Gamage, 1994: Application of structure preserving wavelet decompositions to intermittent turbulence. *Wavelets in Geophysics*, E. Foufoula-Georgiou and P. Kumar, Eds., Academic Press, 45–80.
- Hoegh-Guldberg, O., 1999: Climate change, coral bleaching and the future of the world's coral reefs. *Mar. Freshwater Res.*, **50**, 839–866.
- , and Coauthors, 2007: Coral reefs under rapid climate change and ocean acidification. *Science*, **318**, 1737–1742.
- Jevrejeva, S., J. C. Moore, and A. Grinsted, 2003: Influence of the Arctic Oscillation and El Niño–Southern Oscillation (ENSO) on ice conditions in the Baltic Sea: The wavelet approach. *J. Geophys. Res.*, **108**, 4677, doi:10.1029/2003JD003417.
- Katul, G., and B. Vidakovic, 1996: The partitioning of attached and detached eddy motion in the atmospheric surface layer using Lorentz wavelet filtering. *Bound.-Layer Meteor.*, **77**, 153–172.
- , and —, 1998: Identification of low-dimensional energy containing flux transporting eddy motion in the atmospheric surface layer using wavelet thresholding methods. *J. Atmos. Sci.*, **55**, 377–389.
- Kumar, P., and E. Foufoula-Georgiou, 1994: Wavelet analysis in geophysics: An introduction. *Wavelet Analysis and Its Applications*, E. Foufoula-Georgiou and P. Kumar, Eds., Vol. 4, *Wavelets in Geophysics*, Academic Press, 1–43.
- Lesser, M. P., 2004: Experimental biology of coral reef ecosystems. *J. Exp. Mar. Biol. Ecol.*, **300**, 217–252.
- Oke, T. R., 1987: *Boundary Layer Climates*. Methuen, 435 pp.
- Perry, A., and J. Li, 1990: Experimental support for the attached-eddy hypothesis in zero-pressure gradient turbulence boundary layers. *J. Fluid Mech.*, **218**, 405–438.
- , S. Henbest, and M. Chong, 1986: A theoretical and experimental study of wall turbulence. *J. Fluid Mech.*, **165**, 163–199.
- Salmond, J. A., 2005: Wavelet analysis of intermittent turbulence in a very stable nocturnal boundary layer: Implications for the vertical mixing of ozone. *Bound.-Layer Meteor.*, **114**, 463–488.
- Smith, N. P., 2001: Weather and hydrographic conditions associated with coral bleaching: Lee Stocking Island, Bahamas. *Coral Reefs*, **20**, 415–422.
- Solomon, S., D. Qin, M. Manning, Z. Chen, M. Marquis, K. B. Averyt, M. Tignor, and H. L. Miller, Eds., 2007: *Climate Change 2007: The Physical Science Basis*. Cambridge University Press, 996 pp.
- Stull, R., 1998: *An Introduction to Boundary Layer Meteorology*. Kluwer Academic Publishers, 666 pp.
- Sun, X.-M., Z.-L. Zhu, X.-F. Wen, G.-F. Yuan, and G.-R. Yu, 2006: The impact of averaging period on eddy fluxes observed at ChinaFLUX sites. *Agric. For. Meteorol.*, **137**, 188–193.
- Szilagyi, J., M. B. Parlange, G. G. Katul, and J. D. Albertson, 1999: An objective method for determining principal time scales of coherent eddy structures using orthonormal wavelets. *Adv. Water Resour.*, **22**, 561–566.
- Thomas, C., and T. Foken, 2005: Detection of long-term coherent exchange over spruce forest using wavelet analysis. *Theor. Appl. Climatol.*, **80**, 91–104.
- , and —, 2007: Organised motion in a tall spruce canopy: Temporal scales, structure spacing and terrain effects. *Bound.-Layer Meteor.*, **122**, 123–147.
- Torrence, C., and G. P. Compo, 1998: A practical guide to wavelet analysis. *Bull. Amer. Meteor. Soc.*, **79**, 61–78.
- Townsend, A., 1976: *The Structure of Turbulent Shear Flow*. Cambridge University Press, 429 pp.
- Voronovich, V., and G. Kiely, 2007: On the gap in the spectra of surface-layer atmospheric turbulence. *Bound.-Layer Meteor.*, **122**, 67–83.
- Zeng, X., R. A. Pielke, and R. Eykholt, 1993: Chaos theory and its applications to the atmosphere. *Bull. Amer. Meteor. Soc.*, **74**, 631–644.